

# Electric Gap Characterization at Mesoscopic Scale with Scanning Probe Microscopy

**Dian Li**

University of Hong Kong <https://orcid.org/0000-0002-8477-7962>

**Xiong Wang**

University of Hong Kong

**Xiaoyong Mo**

University of Hong Kong

**Edmund Tse**

University of Hong Kong <https://orcid.org/0000-0002-9313-1290>

**Xiaodong Cui** (✉ [xdcui@hku.hk](mailto:xdcui@hku.hk))

University of Hong Kong <https://orcid.org/0000-0002-2013-8336>

---

## Article

**Keywords:** scanning probe microscopy, electric force microscopy, quantum capacitance, bandgap characterization, band alignment

**Posted Date:** March 24th, 2022

**DOI:** <https://doi.org/10.21203/rs.3.rs-1461674/v1>

**License:**   This work is licensed under a Creative Commons Attribution 4.0 International License.

[Read Full License](#)

---

**Version of Record:** A version of this preprint was published at Nature Communications on August 8th, 2022. See the published version at <https://doi.org/10.1038/s41467-022-32439-1>.

# Abstract

We develop a scanning probe microscopic technique to characterize the electric gap with a spatial resolution of nanometre scale. The technique probes the electric gap by monitoring the change of the local quantum capacitance via the Coulomb force at the mesoscopic scale. We showcase this technique on several 2D semiconductors and van der Waals heterostructures at ambient conditions.

## Full Text

Electric gaps, either bandgap for crystals or highest occupied molecular orbital-lowest unoccupied molecular orbital (HOMO-LUMO) gap for molecular systems play a dominating role in material electric properties. Although there are various experimental techniques from photoemission<sup>1</sup> and optical spectroscopy<sup>2</sup> to electric transports,<sup>3</sup> it is still challenging to realize electric gap characterization with nanometre spatial resolution. Despite great development and extension of the scanning probe microscopy (SPM),<sup>4</sup> the scanning tunneling spectroscopy (STS),<sup>5-8</sup> a working mode of scanning microscopy (STM),<sup>9</sup> is probably the only widely used technique capable of probing the electric gap with a nanometre resolution. Generally, STS provides the differential conductance  $dI/dV$  of the tunneling current as a function of the fermi level difference between the sample and the sharp metal tip. This differential conductance  $dI/dV$  reflects the electron's local density of states (LDOS) and therefore the gap state could be extracted. The atomic resolution of STM makes STS a gap characterizing tool with ultimate spatial resolution. However, STS suffers many limitations inherited from STM. It works only on fairly conducting samples and substrates. As the tunneling current exponentially depends on the spatial separation between the STM tip and samples, any mechanical vibration even thermal fluctuation blurs the needed information. This limits the application of STS only viable at cryogenic temperature. In this article we demonstrate a new technique of SPM for electric gap characterization with nanometre spatial resolution while immune to the environmental restrictions. The technique scrutinizes the local electric field as a function of the Fermi energy difference between the sample and the conductive atomic force microscopy (AFM) tip and subsequently extracts the electric gap from the measured local quantum capacitance fluctuation. The nature of the long-range Coulomb field relaxes the strict requirement on environmental stabilities and makes this technique applicable at ambient conditions.

In regular electric force microscopy (EFM)<sup>10</sup> charge transfer aligns the Fermi or quasi-Fermi level between samples and the conductive AFM tip, and consequently shifts the local surface vacuum levels by a so-called contact potential difference,  $V_{CPD}$ , which reflects the energy difference between the (quasi) Fermi levels of the tip and the sample. This  $V_{CPD}$  builds a local electric field between the samples and the tip (Fig. 1b). This electric field

could be probed with the Coulomb force acting on the conductive AFM tip as sketched in Fig. 1a. Generally, under an external bias  $V_{\text{bias}}$  between the sample and the tip (Fig. 1c & d), the electrostatic energy  $U_{\text{el}}$  of the entire system could be simply described by a charging capacitor model

$$U_{\text{el}}(z, V_{\text{bias}}) = -\frac{1}{2}C_s(z)(V_{\text{bias}} + V_{\text{CPD}})^2 \quad (1)$$

where the capacitance  $C_s$  is the effective capacitance of the entire system. In a simple but realistic model,<sup>11,12</sup> the electrostatic capacitance is

$$C_s(z) = 2\pi\epsilon_0\epsilon_r R_{\text{tip}} \ln\left(1 + \frac{R_{\text{tip}}}{z}\right) \quad (2)$$

where the capacitor is built up with the tip modeled by a conductor cone with an apex curve of  $R_{\text{tip}}$  and the sample modeled by a semi-infinite plane, and the separation between them is  $z$  (Fig. 1e). The electrostatic force added on the tip could be described by the negative gradient of  $U_{\text{el}}$ , i.e.,

$$F_{\text{el}}(z, V) = -\frac{\partial U_{\text{el}}(z)}{\partial z} = \frac{1}{2} \frac{\partial C_s(z)}{\partial z} (V_{\text{bias}} + V_{\text{CPD}})^2 \quad (3)$$

If we scan the external bias, the electrostatic force displays a parabolic curve as sketched in Fig. 2a. The contact potential could be extracted easily from the bias voltage corresponding to the maximum of the force vs. external bias curve.<sup>13</sup> This is similar to how the scanning Kelvin probe microscopy works.<sup>14</sup> If the tip is close enough to the sample where the Coulomb field is dominated by the local mesoscopic area (Fig. 1f), the quantum states to accommodate extra electrons(holes) in the sample's domain are limited owing to its finite LDOS. Namely, the finite electron states owing to the limited LDOS in a mesoscopic volume affects the system capacitance with a form of quantum capacitance,

$$C_q(u) = \frac{dQ(u)}{du} = Ae \int_0^\infty \frac{\partial f(V-u)}{\partial u} \text{DOS}(V) dV \quad (4)$$

where  $A$  is the area or volume of the system depending on a 2D or 3D case while  $e$  and  $f(\epsilon)$  are the electron charge and the Fermi-Dirac distribution function, respectively. The quantum capacitance in mesoscopic islands decreases as the effective area/volume shrinks.

If  $C_q$  is comparable with  $C_e$ , the quantum capacitance kicks in the Coulomb force. The system capacitance is the combination of both electrostatic capacitance and the quantum

capacitance of the local domain, say  $C_s = \frac{C_e C_q}{C_e + C_q}$ . The definition of quantum capacitance (Eq. 4) implies that the quantum capacitance drops to zero at zero temperature or close to zero at finite temperature when the Fermi level is within the energy gap. Namely, if the external bias pushes the Fermi

level within the energy gap at the sample, there is no vacancy to accommodate extra charge transfer between the tip and the sample and consequently, the local electric field is pinned down. Theoretically, under this proposed EFM working mode, one can predict that the force vs. external bias curve could reflect the LDOS and consequently reveal the electric gap of the sample at the local domain. For the sake of distinction, we use LEFM (localized electric force microscopy) to distinguish the proposed EFM working mode from regular EFM.

Fig. 2a & c shows a paradigm of the regular EFM working mode on the most common monolayer transition metal dichalcogenide (TMDC) MoS<sub>2</sub> on indium tin oxide (ITO) glasses. Under the regular EFM mode (dynamic force/non-contact mode under a small AC bias), the vibration amplitude which reflects the force added on the tip displays a parabolic response to the external bias as shown in Fig. 2c. The parabolic response is further enhanced as we reduce the separation between the tip and the sample Fig. 2a. It is fully expected in classical electrostatics (Eq. 2 & 3). When the separation is in the range of 32-42 nm, however, the electrostatic force shows an irresponsive gap state under small bias ranges across all the nanoflakes (Fig. 2b). A gap of 2.28eV is observed on monolayer MoS<sub>2</sub> which is consistent with its electronic bandgap.<sup>3,15</sup> We attribute this irresponsive gap to the bandgap of nanoflakes. As the sample is biased lower than -1.244eV (higher than +1.04eV), the Fermi level of the tip lies in the valance (conduction) band of monolayer MoS<sub>2</sub> and the adequate DOS provides sufficient vacancy for carriers, and consequently, electric field builds up (Fig 1h & f). Whereas, when the bias is set between -1.244eV and 1.04eV, the tip Fermi level is within the bandgap of monolayer MoS<sub>2</sub>, the zero DOS in the gap leads to tiny quantum capacitance in the gap state at finite temperature as illustrated in Eq. 4. Therefore, the charge transfer cannot classically take place, and this is reflected in the electrostatic field on the tip (Fig. 1g). When the separation keeps reducing in this range, the length of the platform keeps constant while the amplitude of the curve keeps growing (Fig. 2d). After that, when the separation reduces to under 30 nm, the curve starts to be chaotic, and this may be related to the fact that the repulsive van der Waals force dominates at such a short distance.

We demonstrate this technique in detecting the band edges of various 2D semiconductors and heterostructures. Fig. 3(a)-(d) shows the representative band edges of monolayer, bilayer, and multilayer (with thickness around 20-40 nm) of these four TMDCs (MoS<sub>2</sub>, MoSe<sub>2</sub>, WS<sub>2</sub>, and WSe<sub>2</sub>) on ITO glasses. The statistical experimental results are summarised in Fig. 3(e) and Table S1. All the results are consistent with the experimental reports with other techniques (Fig. 3e). This well verifies the reliability of our LEFM technique.

The bandgap probed by this technique reflects the electronic bandgap. We could extract the exciton binding energy with the optical band gap which could be obtained by photoluminescence (PL) spectroscopy on the same sample. The exciton binding energy can be estimated by the energy difference between the optical gap and the electronic gap. The PL spectroscopy could be found at SI. Our results are summarised in Table 1 and the exciton binding energies are consistent with the former reports.

**Table 1.** The measured optical band gap (direct/indirect optical gap for bilayer sample) by photoluminescence spectroscopy and the corresponding exciton binding energy of four common TMDCs in monolayer and bilayer. The related former reported results are listed for comparison.

Unit (eV)		measured optical gap	formerly reported	exciton binding energy	formerly reported
MoS <sub>2</sub>	monolayer	1.891	1.81~1.9 <sup>16,17,29</sup>	0.352	0.09~0.57 <sup>3,16,17,30,31</sup>
	bilayer	1.88/1.60	1.59~1.6 <sup>29,32</sup>	0.311	
MoSe <sub>2</sub>	monolayer	1.575	1.56~1.65 <sup>7,23,33,34</sup>	0.641	0.59 <sup>23</sup>
	bilayer	1.57/1.52	1.55 <sup>23,33,34</sup>	0.142	0.21 <sup>23</sup>
WS <sub>2</sub>	monolayer	2.021	2.02~2.09 <sup>25,26</sup>	0.611	0.32~0.71 <sup>17,25,26,30,35</sup>
	bilayer	1.99/1.76	1.68~1.73 <sup>26,36</sup>	0.45	
WSe <sub>2</sub>	monolayer	1.647	1.61~1.735 <sup>16,23,34,37</sup>	0.618	0.14~0.655 <sup>16,23,37,38</sup>
	bilayer	1.64/1.43	1.54~1.605 <sup>23,34</sup>	0.377	0.23 <sup>23</sup>

This technique also provides a versatile tool to study the band edge profile with nanometre resolution. Fig. 4 exhibits this technique in characterizing band alignment in a van der Waals heterostructure of monolayer MoSe<sub>2</sub>/WSe<sub>2</sub>. The band edge profile could be mapped at the ambient condition as shown in Fig. 4c. A clear type II bandgap alignment is identified on the area of the heterostructure, and this result is consistent with other experiment reports elsewhere.<sup>39-42</sup>

In summary, we demonstrate an extended EFM technique that can detect the energy gap profile of various 2D semiconductors and van der Waals heterostructures with nanometre resolution at ambient conditions.

## References

- 1 Huang, Y. L. *et al.* Bandgap tunability at single-layer molybdenum disulphide grain boundaries. *Nature Communications* **6**, 6298, doi:10.1038/ncomms7298 (2015).
- 2 Zhao, W., Ribeiro, R. M. & Eda, G. Electronic Structure and Optical Signatures of Semiconducting Transition Metal Dichalcogenide Nanosheets. *Accounts of Chemical Research* **48**, 91-99, doi:10.1021/ar500303m (2015).
- 3 Zhang, C., Johnson, A., Hsu, C.-L., Li, L.-J. & Shih, C.-K. Direct Imaging of Band Profile in Single Layer MoS<sub>2</sub> on Graphite: Quasiparticle Energy Gap, Metallic Edge States, and Edge Band Bending. *Nano Letters* **14**, 2443-2447, doi:10.1021/nl501133c (2014).
- 4 Bian, K. *et al.* Scanning probe microscopy. *Nature Reviews Methods Primers* **1**, 36, doi:10.1038/s43586-021-00033-2 (2021).
- 5 Feenstra, R. M. Scanning tunneling spectroscopy. *Surface Science* **299-300**, 965-979, doi:10.1016/0039-6028(94)90710-2 (1994).

- 6 Hamers, R. J., Tromp, R. M. & Demuth, J. E. Surface Electronic Structure of Si (111)-(7×7) Resolved in Real Space. *Physical Review Letters* **56**, 1972-1975, doi:10.1103/PhysRevLett.56.1972 (1986).
- 7 Hess, H. F., Robinson, R. B., Dynes, R. C., Valles, J. M. & Waszczak, J. V. Scanning-Tunneling-Microscope Observation of the Abrikosov Flux Lattice and the Density of States near and inside a Fluxoid. *Physical Review Letters* **62**, 214-216, doi:10.1103/PhysRevLett.62.214 (1989).
- 8 Chen, C. J. Theory of scanning tunneling spectroscopy. *Journal of Vacuum Science & Technology A* **6**, 319-322, doi:10.1116/1.575444 (1988).
- 9 Binnig, G., Rohrer, H., Gerber, C. & Weibel, E. Surface Studies by Scanning Tunneling Microscopy. *Physical Review Letters* **49**, 57-61, doi:10.1103/PhysRevLett.49.57 (1982).
- 10 Xu, S. & Arnsdorf, M. F. Electrostatic force microscope for probing surface charges in aqueous solutions. *Proceedings of the National Academy of Sciences* **92**, 10384-10388, doi:10.1073/pnas.92.22.10384 (1995).
- 11 Saint Jean, M., Hudlet, S., Guthmann, C. & Berger, J. Van der Waals and capacitive forces in atomic force microscopies. *Journal of Applied Physics* **86**, 5245-5248, doi:10.1063/1.371506 (1999).
- 12 Hudlet, S., Saint Jean, M., Guthmann, C. & Berger, J. Evaluation of the capacitive force between an atomic force microscopy tip and a metallic surface. *The European Physical Journal B - Condensed Matter and Complex Systems* **2**, 5-10, doi:10.1007/s100510050219 (1998).
- 13 Cui, X. D. *et al.* Bias-induced forces in conducting atomic force microscopy and contact charging of organic monolayers. *Ultramicroscopy* **92**, 67-76, doi:10.1016/S0304-3991(02)00069-4 (2002).
- 14 Nonnenmacher, M., O'Boyle, M. P. & Wickramasinghe, H. K. Kelvin probe force microscopy. *Applied Physics Letters* **58**, 2921-2923, doi:10.1063/1.105227 (1991).
- 15 Hill, H. M., Rigosi, A. F., Rim, K. T., Flynn, G. W. & Heinz, T. F. Band Alignment in MoS<sub>2</sub>/WS<sub>2</sub> Transition Metal Dichalcogenide Heterostructures Probed by Scanning Tunneling Microscopy and Spectroscopy. *Nano Letters* **16**, 4831-4837, doi:10.1021/acs.nanolett.6b01007 (2016).
- 16 Park, S. *et al.* Direct determination of monolayer MoS<sub>2</sub> and WSe<sub>2</sub> exciton binding energies on insulating and metallic substrates. *2D Materials* **5**, 025003, doi:10.1088/2053-1583/aaa4ca (2018).
- 17 Rigosi, A. F., Hill, H. M., Rim, K. T., Flynn, G. W. & Heinz, T. F. Electronic band gaps and exciton binding energies in monolayer Mo<sub>x</sub>W<sub>1-x</sub>S<sub>2</sub> transition metal dichalcogenide alloys probed by scanning tunneling and optical spectroscopy. *Physical Review B* **94**, 075440, doi:10.1103/PhysRevB.94.075440 (2016).

- 18 Beal, A. R. & Hughes, H. P. Kramers-Kronig analysis of the reflectivity spectra of 2H-MoS<sub>2</sub>, 2H-MoSe<sub>2</sub> and 2H-MoTe<sub>2</sub>. *Journal of Physics C: Solid State Physics* **12**, 881-890, doi:10.1088/0022-3719/12/5/017 (1979).
- 19 Bradley, A. J. *et al.* Probing the Role of Interlayer Coupling and Coulomb Interactions on Electronic Structure in Few-Layer MoSe<sub>2</sub> Nanostructures. *Nano Letters* **15**, 2594-2599, doi:10.1021/acs.nanolett.5b00160 (2015).
- 20 Zhang, Q. *et al.* Bandgap renormalization and work function tuning in MoSe<sub>2</sub>/hBN/Ru(0001) heterostructures. *Nature Communications* **7**, 13843, doi:10.1038/ncomms13843 (2016).
- 21 Ugeda, M. M. *et al.* Giant bandgap renormalization and excitonic effects in a monolayer transition metal dichalcogenide semiconductor. *Nature Materials* **13**, 1091-1095, doi:10.1038/nmat4061 (2014).
- 22 Barja, S. *et al.* Charge density wave order in 1D mirror twin boundaries of single-layer MoSe<sub>2</sub>. *Nature Physics* **12**, 751-756, doi:10.1038/nphys3730 (2016).
- 23 Liu, H. J. *et al.* Molecular-beam epitaxy of monolayer and bilayer WSe<sub>2</sub>: a scanning tunneling microscopy/spectroscopy study and deduction of exciton binding energy. *2D Materials* **2**, 034004, doi:10.1088/2053-1583/2/3/034004 (2015).
- 24 Jo, S., Ubrig, N., Berger, H., Kuzmenko, A. B. & Morpurgo, A. F. Mono- and Bilayer WS<sub>2</sub> Light-Emitting Transistors. *Nano Letters* **14**, 2019-2025, doi:10.1021/nl500171v (2014).
- 25 Zhu, B., Chen, X. & Cui, X. Exciton Binding Energy of Monolayer WS<sub>2</sub>. *Scientific Reports* **5**, 9218, doi:10.1038/srep09218 (2015).
- 26 Chernikov, A. *et al.* Exciton Binding Energy and Nonhydrogenic Rydberg Series in Monolayer WS<sub>2</sub>. *Physical Review Letters* **113**, 076802, doi:10.1103/PhysRevLett.113.076802 (2014).
- 27 Kobayashi, Y. *et al.* Modulation of electrical potential and conductivity in an atomic-layer semiconductor heterojunction. *Scientific Reports* **6**, 31223, doi:10.1038/srep31223 (2016).
- 28 Braga, D., Gutiérrez Lezama, I., Berger, H. & Morpurgo, A. F. Quantitative Determination of the Band Gap of WS<sub>2</sub> with Ambipolar Ionic Liquid-Gated Transistors. *Nano Letters* **12**, 5218-5223, doi:10.1021/nl302389d (2012).
- 29 Mak, K. F., Lee, C., Hone, J., Shan, J. & Heinz, T. F. Atomically Thin MoS<sub>2</sub>: A New Direct-Gap Semiconductor. *Physical Review Letters* **105**, 136805, doi:10.1103/PhysRevLett.105.136805 (2010).
- 30 Hill, H. M. *et al.* Observation of Excitonic Rydberg States in Monolayer MoS<sub>2</sub> and WS<sub>2</sub> by Photoluminescence Excitation Spectroscopy. *Nano Letters* **15**, 2992-2997, doi:10.1021/nl504868p (2015).

- 31 Klots, A. R. *et al.* Probing excitonic states in suspended two-dimensional semiconductors by photocurrent spectroscopy. *Scientific Reports* **4**, 6608, doi:10.1038/srep06608 (2014).
- 32 Newaz, A. K. M. *et al.* Electrical control of optical properties of monolayer MoS<sub>2</sub>. *Solid State Communications* **155**, 49-52, doi:10.1016/j.ssc.2012.11.010 (2013).
- 33 Tongay, S. *et al.* Thermally Driven Crossover from Indirect toward Direct Bandgap in 2D Semiconductors: MoSe<sub>2</sub> versus MoS<sub>2</sub>. *Nano Letters* **12**, 5576-5580, doi:10.1021/nl302584w (2012).
- 34 Tonndorf, P. *et al.* Photoluminescence emission and Raman response of monolayer MoS<sub>2</sub>, MoSe<sub>2</sub>, and WSe<sub>2</sub>. *Opt. Express* **21**, 4908-4916, doi:10.1364/OE.21.004908 (2013).
- 35 Ye, Z. *et al.* in *Frontiers in Optics 2014*. LW2I.4 (Optica Publishing Group).
- 36 Zhu, B., Zeng, H., Dai, J., Gong, Z. & Cui, X. Anomalously robust valley polarization and valley coherence in bilayer WS<sub>2</sub>. *Proceedings of the National Academy of Sciences* **111**, 11606-11611, doi:10.1073/pnas.1406960111 (2014).
- 37 He, K. *et al.* Tightly Bound Excitons in Monolayer WSe<sub>2</sub>. *Physical Review Letters* **113**, 026803, doi:10.1103/PhysRevLett.113.026803 (2014).
- 38 Wang, G. *et al.* Giant Enhancement of the Optical Second-Harmonic Emission of WSe<sub>2</sub> Monolayers by Laser Excitation at Exciton Resonances. *Physical Review Letters* **114**, 097403, doi:10.1103/PhysRevLett.114.097403 (2015).
- 39 Rivera, P. *et al.* Observation of long-lived interlayer excitons in monolayer MoSe<sub>2</sub>-WSe<sub>2</sub> heterostructures. *Nature Communications* **6**, 6242, doi:10.1038/ncomms7242 (2015).
- 40 Rigosi, A. F., Hill, H. M., Li, Y., Chernikov, A. & Heinz, T. F. Probing Interlayer Interactions in Transition Metal Dichalcogenide Heterostructures by Optical Spectroscopy: MoS<sub>2</sub>/WS<sub>2</sub> and MoSe<sub>2</sub>/WSe<sub>2</sub>. *Nano Letters* **15**, 5033-5038, doi:10.1021/acs.nanolett.5b01055 (2015).
- 41 Calman, E. V. *et al.* Indirect Excitons and Trions in MoSe<sub>2</sub>/WSe<sub>2</sub> van der Waals Heterostructures. *Nano Letters* **20**, 1869-1875, doi:10.1021/acs.nanolett.9b05086 (2020).
- 42 Wang, Z. *et al.* Phonon-Mediated Interlayer Charge Separation and Recombination in a MoSe<sub>2</sub>/WSe<sub>2</sub> Heterostructure. *Nano Letters* **21**, 2165-2173, doi:10.1021/acs.nanolett.0c04955 (2021).

## Declarations

**Supplementary Information** is available for this paper.

**Acknowledgments:** This work was supported by MOST 2020YFA0309603 of the Ministry of Science and Technology of the People's Republic of China; Croucher Foundation; GRF #17304518, CRF C7036-17W and AoE/P-701/20 of the Research Grant Council of Hong Kong. DL and XW thank Dr. Yipu Xia and Prof. Maohai Xie for providing the conductive silicon carbide substrate.

**Author contributions:** XC conceived and supervised the project. DL conducted the experiments and analyzed the data. DL and XW fabricated the sample. XM and ET provide support on AFM. DL and XC wrote the paper.

**Competing interests:** Authors declare no competing interests.

## Methods

### Sample preparation

The few-layer TMDC samples were cleaved from the single crystal via mechanical exfoliation method by using the Scotch tape and then directly transfer to a conductive substrate like ITO glasses. For van der Waal heterostructures, monolayer samples were exfoliated severally onto a silicon substrate and the thickness was confirmed by the AFM topography mapping. Then the heterostructure was fabricated via the hot pick-up technique<sup>43</sup> and eventually transfer to a flat conductive silicon carbide substrate.

### LEFM scanning

After the topography mapping of the sample, we move the AFM tip to the area we are interested in, retrace the tip with 50 nm, and then disable the z-feedback controller to maintain a constant tip-sample distance and start the regular EFM scanning. The scanning bias voltage is in the range of -2 V to 2 V. Then adjust the tip-sample distance to get an evident vibration amplitude-external bias curve. For the 2D TMDCs sample, this distance is around 44 nm. After getting an evident vibration amplitude-external bias curve from the regular EFM scanning, we decrease the height of the cantilever every 2 nm and monitor the change of the vibration amplitude-external bias curve. The platform-like curve is shown out when the tip-sample distance is in the range of 32-42 nm. The scanning bias voltage is the same as the regular EFM scanning.

### Photoluminescence measurement

Photoluminescence measurement was conducted with a homemade PL measurement system with a 532nm continuous excitation laser. The laser was focused on the sample with a micron-size spot ( $\phi \sim 3\mu\text{m}$ ) and the intensity was around  $2\text{ W/cm}^2$ .

## References

43 Pizzocchero, F. *et al.* The hot pick-up technique for batch assembly of van der Waals heterostructures. *Nature Communications* **7**, 11894, doi:10.1038/ncomms11894 (2016).

# Figures

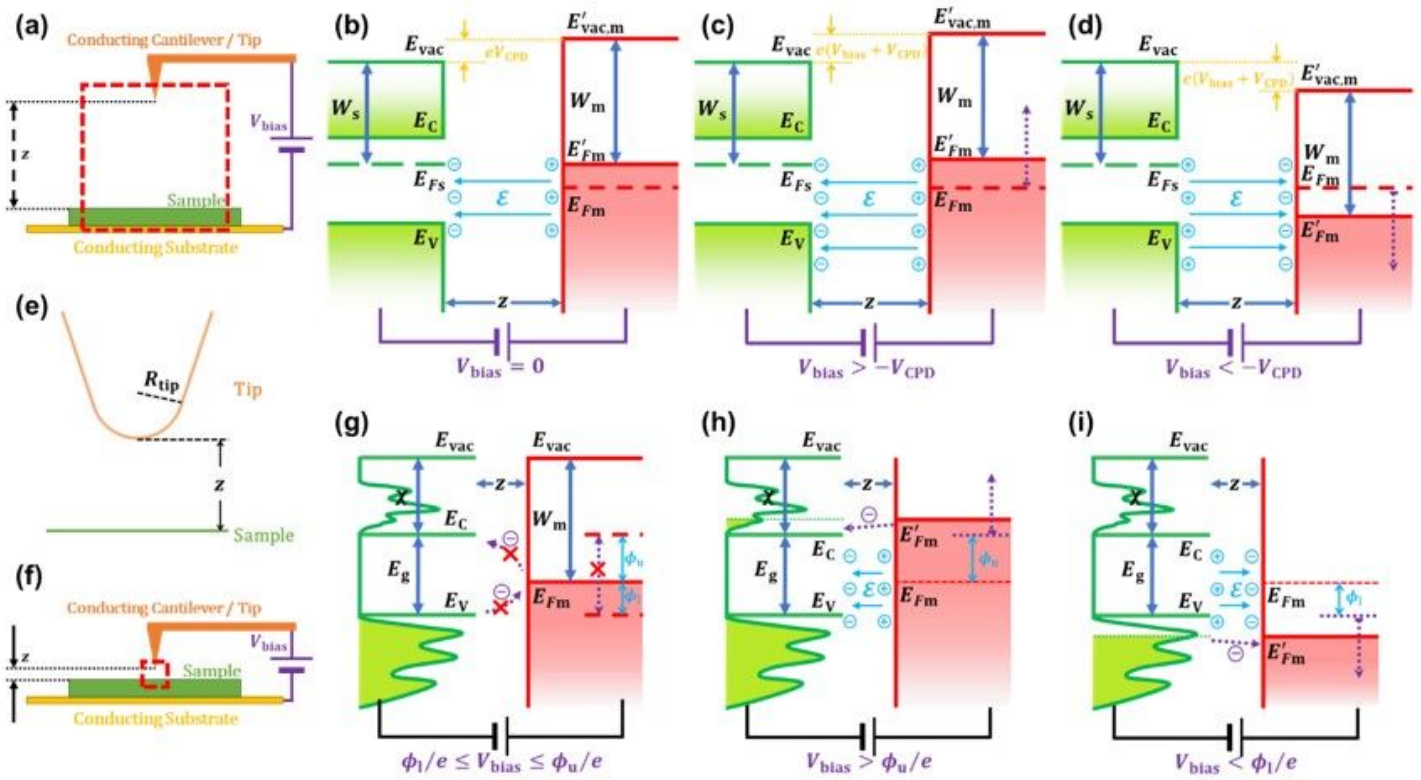
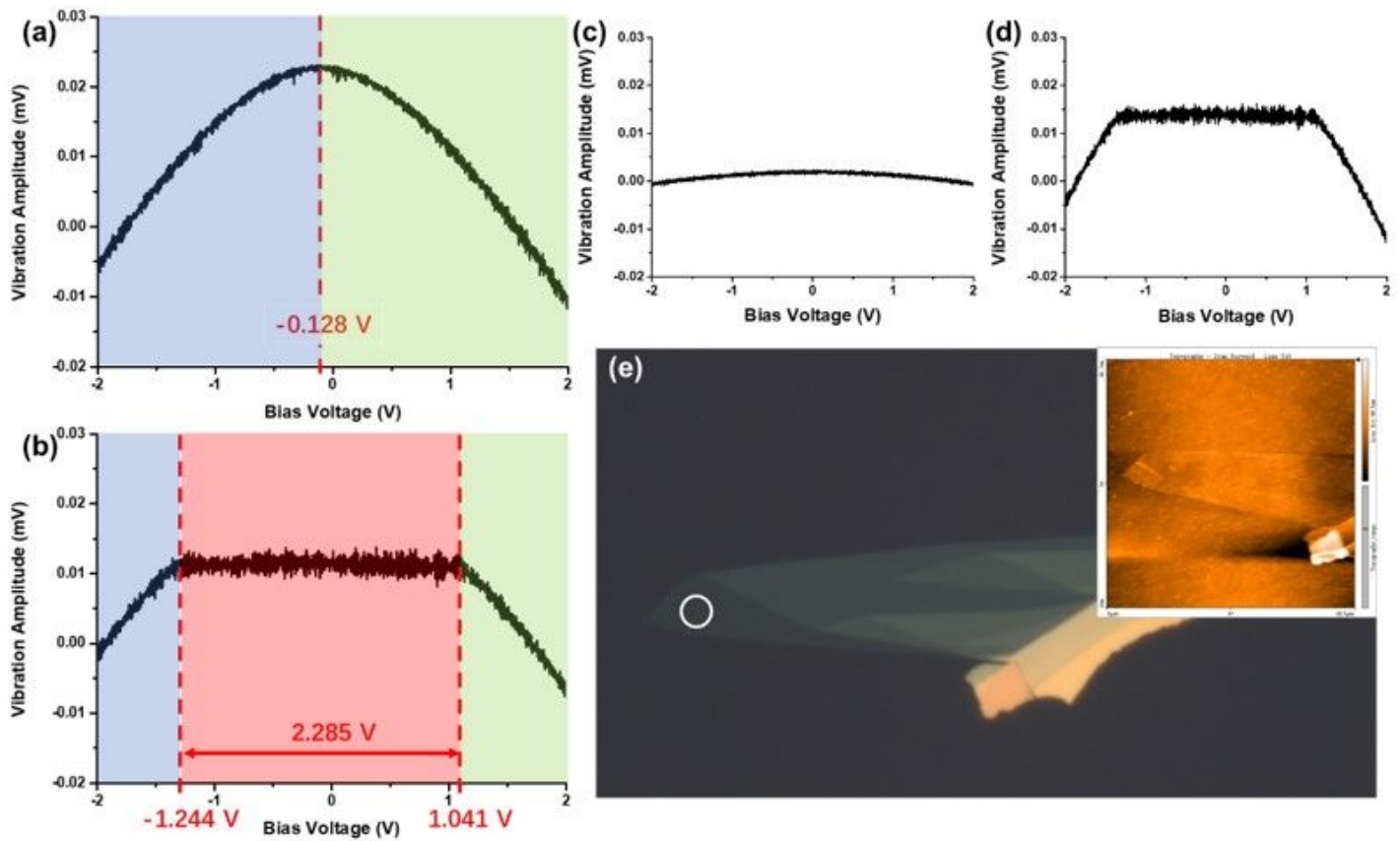


Figure 1

The schematic diagram of (a) the regular EFM where the local electric field is monitored by the Coulomb force on the conductive AFM tip, and (f) the LEFM that the local quantum capacitance plays a significant role at a close tip-sample distance. The energy level alignment between the conductive tip and the sample at (b-d) the regular EFM and (g-i) the LEFM under various bias voltages. (e) The capacitor model of the system is composed of the conductive AFM tip and the sample plane.



**Figure 2**

The curve of vibration amplitude vs. external bias on monolayer MoS<sub>2</sub> area (circled in white in (e)) obtained by the regular EFM or LEFM technique with the separation between the tip and the sample of (c) 50 nm, (a) 44 nm, (b) 40 nm, and (d) 36 nm, respectively. (e) the optical image of the few-layer MoS<sub>2</sub> on an ITO substrate. The inset is the corresponding AFM topography mapping.

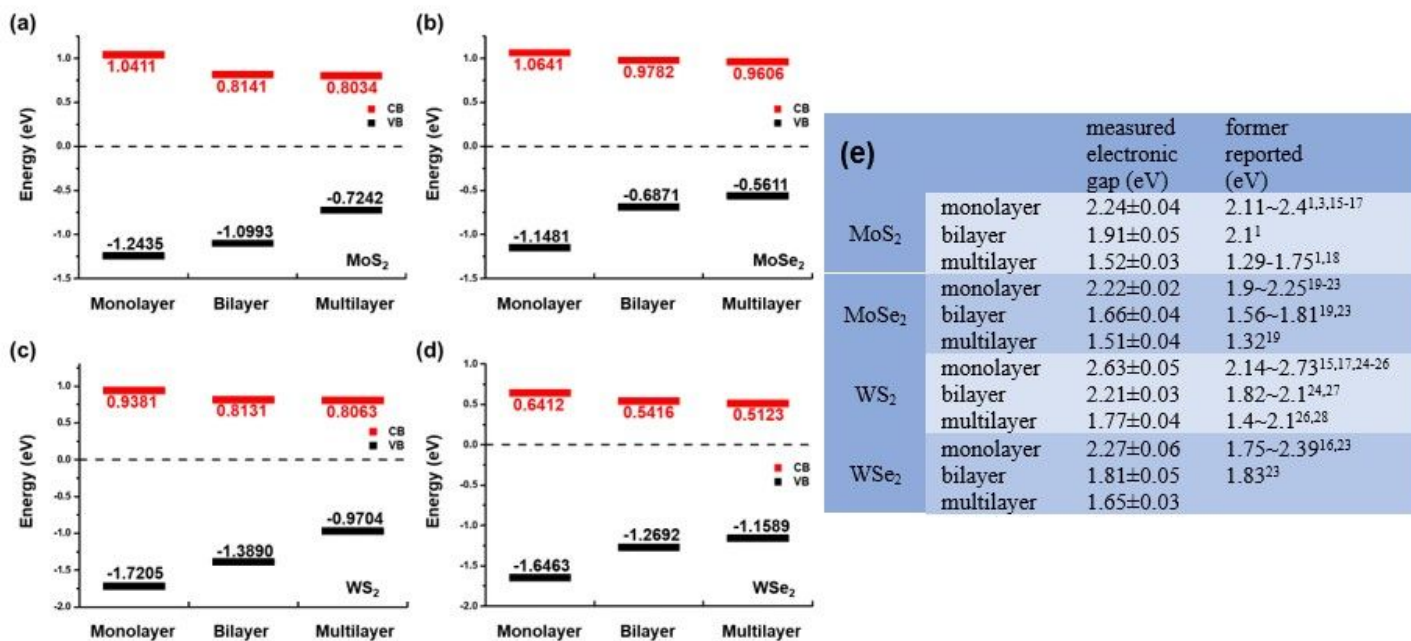
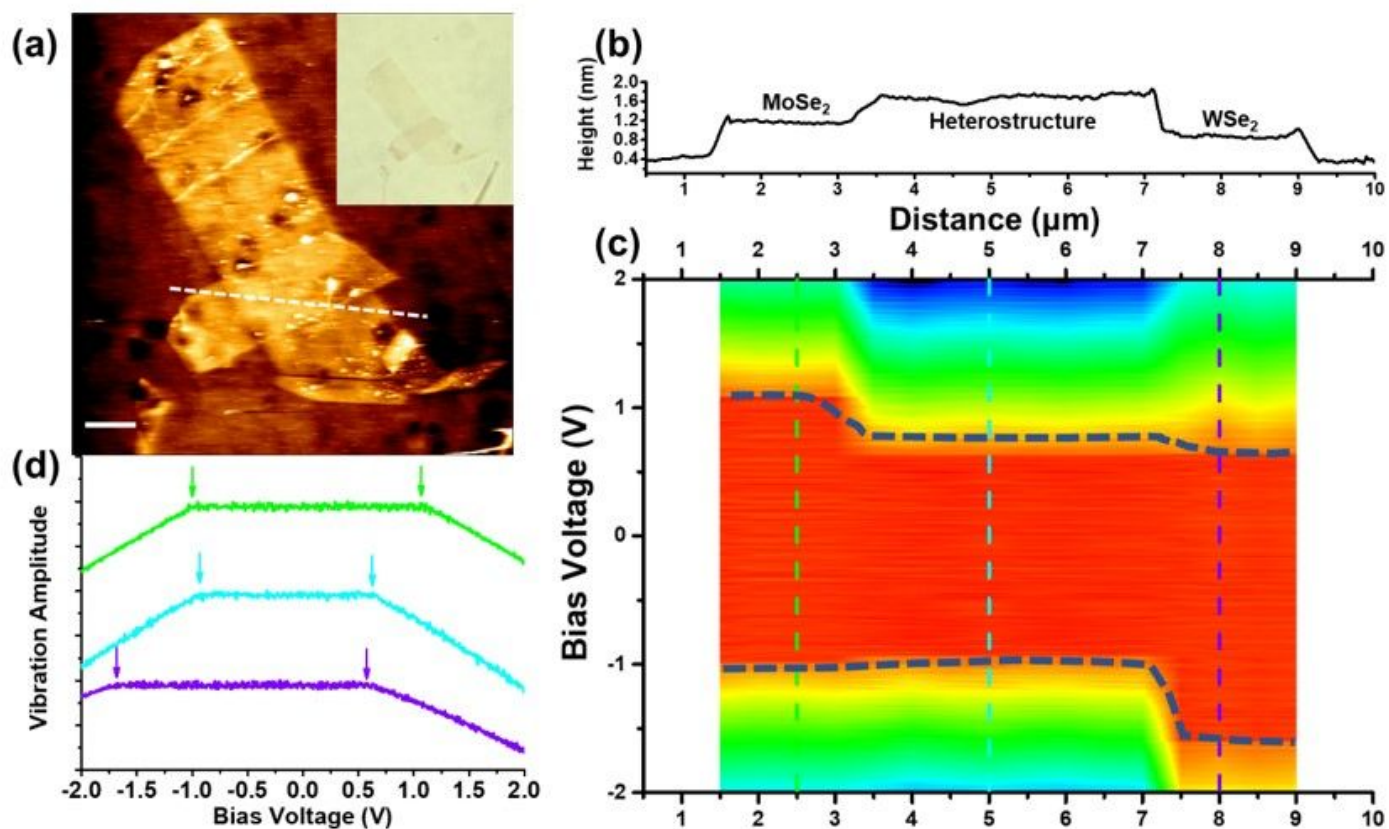


Figure 3

The layer-dependent electronic bandgap of (a) MoS<sub>2</sub>, (b) MoSe<sub>2</sub>, (c) WS<sub>2</sub>, and (d) WSe<sub>2</sub> revealed by the LEFM technique. (e) The statistical results and comparison with the reports by other techniques.



**Figure 4**

(a) AFM topography mapping of the MoSe<sub>2</sub>/ WSe<sub>2</sub> van der Waals heterostructure (scale bar 2μm). Inset is the optical image of the same sample. (b) The height profile along the white dash line in (a). (c) The band profile of the heterostructure along the white dash line in (a). (d) The vibration amplitude vs. external bias curve is extracted from the dashed line in (c).

## Supplementary Files

This is a list of supplementary files associated with this preprint. Click to download.

- [Sl.docx](#)